文章编号：1000-5773(2013)02-0277-10

Two and Three Dimensional Numerical Investigations of the Single-Mode Richtmyer-Meshkov Instability*

WANG Tao[1,2], BAI Jin-Song[1], LI Ping[1], TAO Gang[2], JIANG Yang[1], ZHONG Min[1]

(1. *Institute of Fluid Physics, CAEP, Mianyang* 621900, *China*;
2. *School of Energy and Power Engineering, Nanjing University of Science and Technology, Nanjing* 210094, *China*)

Abstract: A high precision numerical algorithm MVPPM (multi-viscous-fluid piecewise parabolic method) is proposed and applied to the multi-viscous-fluid dynamics problems. Several two and three dimensional single-mode Richtmyer-Meshkov instability models with different amplitude and wavelength are numerically simulated by this method. Comparisons show that the evolving of interface is highly sensitive to the initial conditions of perturbation. Both two and three dimensional calculated amplitudes and growth rates of perturbed interface are consistent with the predictions of theoretical models, while the strength of initial perturbation is small. The three dimensional numerical results are identical with the two dimensional ones at the linear stage and larger than the two dimensional ones at the nonlinear stage for the perturbation with the same wavelength and amplitude. Therefore the effects of nonlinearity and three dimensions play a dominant role in the development of Richtmyer-Meshkov instability.

Key words: multi-viscous-fluid piecewise parabolic method; single-mode Richtmyer-Meshkov instability; nonlinearity

CLC number: O354; O357 **Document code**: A

1 Introduction

The interface separating two different fluids is accelerated by shock wave, which is called the Richtmyer-Meshkov instability (RMI)[1-2], and it will induce turbulent mixing. The RMI is of importance in a variety of man-made applications and natural phenomena such as inertial confinement fusion (ICF), high-speed combustion and astrophysics (i. e. supernova explosion) and has gained much attention. The physical mechanism for the occurrence of RMI is the baroclinic vorticity production as a result of the misalignment of the pressure gradient of the shock and the local density gradient at the interface (i. e. $\nabla\rho\times\nabla p\neq 0$). The development of RMI follows four stages[3]. The first stage is a wave bifurcation stage, in which the incident shock wave interacts with the initial perturbed interface and bifurcates into a transmitted shock and a reflected wave. Depending on the material properties of the fluids on both sides of the interface, the reflected wave can be either a shock or a rarefaction wave. The criterion is that when the incident shock interacts with the interface from light fluid to heavy one, the reflected wave is a shock; otherwise it is a rarefaction wave. The second stage is a linear stage. Accelerated by the shock, the perturbation at the interface starts to grow, bubbles and spikes are formed at the

* **Received date**: 2010-12-02; **Revised date**: 2011-05-25
Foundation Item: National Natural Science Foundation of China (11202195, 11072228, 11002129)
Biography: WANG Tao (1979—), male, master, major in computational fluid dynamics. E-mail: wtaoxp@21cn. com

interface. In the linear stage, relative to the wavelength of perturbation, the amplitudes of bubble and spike are small. The third stage is a nonlinear stage, in which the effect of compressibility is less important, and the nonlinearity begins to play a dominant role, the spike grows faster than the bubble and becomes mushroom shaped. The fourth stage is a turbulent mixing stage. In this stage, the umbrella and stem of mushroom shaped fracture and become droplets, two fluids have mixed, and the physics of fluid is more complex than other stages.

The single-mode RMI was first investigated by Richtmyer[1] using linear stability analysis in 1960. He proposed an analytical model (impulsive model) by adapting existing model for the Rayleigh-Taylor instability[4] to predict the linear growth of perturbation, $\dot{a}(t)$. However, the impulsive formula is based on the linear theory, so it is valid only as long as the perturbation remains small, $a(t)\ll\lambda$, i. e. in linear stage. To extend the range of RMI theory beyond the linear regime, Zhang & Sohn[5-7] presented an analytical nonlinear theory using higher-order expansion and Padé approximation to predict the growth of perturbation, which is valid from early to late times. Combining the linear impulsive results with asymptotic growth laws, Sadot *et al*.[8] presented another nonlinear model to capture the evolution of single-mode perturbation from early to late times.

In fact, the RMI was firstly found by simulation, and confirmed by experiment subsequently. However, there are some difficulties when simulating the nonlinear interface instability and turbulent mixing, and a variety of numerical algorithms is used currently. Meyer, Cloutman, *et al*.[9-10] carried out some simulations to predict the greater growth rates than observed in single-interface experiments for singly shocked, sinusoidally perturbed interfaces. Other computations show agreement with the experimental growth rates[11-15] by applying the front-tracking technique and mixing model. At present, it is unrealistic to simulate turbulent mixing by using direct numerical simulation (DNS). Yet large-eddy simulation (LES) is a very effective way to simulate the turbulent mixing, and many mixing characters is made to known in turbulent mixing[16-18]. In order to obtain the detailed interface structures, other techniques such as high precision scheme[19-21], Adaptive Mesh Refinement (AMR)[22-23] are used in simulations. We also proposed a high precision numerical algorithm MVPPM, which is successful in simulations of the RMI[24-25]. In this study, the dependence on initial conditions and the effects of nonlinearity and three dimensions are mainly studied in the development of RMI by using MVPPM.

2 Numerical Algorithm

When considering the viscosity and heat-conduction, the governing equations for multi-viscous-fluid can be written as follows

$$\begin{cases} \dfrac{\partial\rho}{\partial t}+\dfrac{\partial\rho u_j}{\partial x_j}=0 \\ \dfrac{\partial\rho u_i}{\partial t}+\dfrac{\partial\rho u_j u_i}{\partial x_j}=-\dfrac{\partial p}{\partial x_i}+\dfrac{\partial\sigma_{ij}}{\partial x_j} \\ \dfrac{\partial\rho E}{\partial t}+\dfrac{\partial(\rho u_j E+pu_j)}{\partial x_j}=-\dfrac{\partial q_j}{\partial x_j}+\dfrac{\partial(u_i\sigma_{ij})}{\partial x_j} \\ \dfrac{\partial Y^{(s)}}{\partial t}+u_j\dfrac{\partial Y^{(s)}}{\partial x_j}=0 \quad s=1,2,\cdots,N-1 \end{cases} \tag{1}$$

Here, i and j represent the three directions of x, y, z; $\rho, u_k (k=i,j)$, and p are the fluid density, velocity and pressure, respectively; E is the total energy per unit mass; N is the types of fluid, $Y^{(s)}$ is the volume fraction of the s^{th} fluid and satisfies $\sum Y^{(s)}=1$; σ_{ij} is the Newtonian fluid viscosity stress tensor

$$\sigma_{ij}=\mu\left(\frac{\partial u_i}{\partial x_j}+\frac{\partial u_j}{\partial x_i}-\frac{2\delta_{ij}}{3}\frac{\partial u_k}{\partial x_k}\right) \tag{2}$$

where μ is the fluid viscosity; q_j is the energy flux per unit time and space, $q_j=-\lambda\partial T/\partial x_j$, T is the

temperature, λ is the efficient heat-conduction coefficient. The equation of state (EOS) adopts the ideal gas state form.

The physical process, as described by Eq. (1), can be decomposed into three sub-processes, i. e., the calculations of inviscid flux, viscous flux and heat flux by operator splitting technique. The inviscid flux is calculated by multi-fluids PPM. The PPM of two-step Lagrange-Remapping algorithm in one time step can be divided into four steps: (1) the piecewise parabolic interpolation of physical quantities; (2) solving the Riemann problems approximately; (3) marching of the Lagrange equations; (4) remapping the physical quantities back to the stationary Euler meshes. Then the viscous flux and heat flux are calculated based on the computation of inviscid flux by using second-order spatial center difference and two-step Runge-Kutta time marching. Detailed description of algorithm can be obtained in Ref. [24].

3 Results and Discussions

3.1 Two Dimensional Single-Mode RMI

The two dimensional computational model is illustrated in Fig. 1. The size of computational domain is $[0, 540\ \text{mm}] \times [0, 60\ \text{mm}]$ in (x, y) dimensions. The incident air shock with Mach 1.2 travels from left to right (along x direction) and accelerates the single-mode initial perturbed air/SF_6 interface. The sinusoidal interfacial perturbation is given by $x(y) = x_0 + a_0 \sin(ky)$, in which x_0 is the initial equilibrium position, a_0 is the initial amplitude, and k is the wavenumber with $k = 2\pi/\lambda_0$, λ_0 is the initial wavelength. In simulations, the left and right boundaries are inflow/outflow boundaries, respectively; the upper and lower boundaries are periodic. The height in spanwise (y) direction is a wavelength. The computational domain is divided into 36 sub-zones (using 18×2 CPUs) each with 100×100 grids for parallel calculating. The initial properties of SF_6 and air are shown in Table 1.

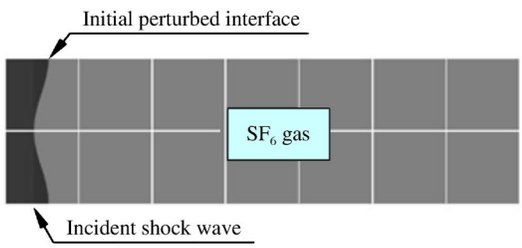


Fig. 1 Two dimensional computational model

Table 1 Initial properties of SF_6 and air

Gas	ρ/(kg/m^3)	p/(MPa)	u/(m/s)	μ/(μPa·s)	γ
SF_6	5.97	0.100	0.000	14.746	1.09
Air	1.18	0.100	0.000	18.526	1.40

The perturbation amplitude and growth rate are calculated as follows in simulations. The definitions of bubble amplitude a_b, spike amplitude a_s and mixing zone width h are illustrated in Fig. 2. The blue contour shows a typical early-time evolution of the interface induced by the RMI from a sinusoidal initial perturbation. The solid red line shows the location of the shocked, unperturbed interface used as a reference for the determination of bubble and spike amplitudes from the numerical data. The distance from the unperturbed interface to the bubble tip is the bubble amplitude a_b, while the distance from the unperturbed interface to the spike tip is the spike amplitude a_s. The mixing zone width h is defined as the sum of bubble and spike amplitudes[10]

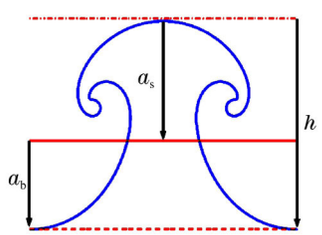


Fig. 2 Schematic of the bubble and spike amplitude, mixing zone width

$$h(t) = a_b(t) + a_s(t) \tag{3}$$

The perturbation amplitude is the average of bubble and spike amplitudes

$$a(t) = [a_b(t) + a_s(t)]/2 \tag{4}$$

i. e., one half the mixing zone width. The corresponding ampli-

tude growth rate is

$$\dot{a}(t) = [\dot{a}_b(t) + \dot{a}_s(t)]/2 = \dot{h}(t)/2 \tag{5}$$

Fifteen models with different amplitude and wavelength are calculated, as listed in Table 2. First, we carried out the convergence test of the numerical solution for grid. The test is completed in two dimensional problems since the mathematical equations and the numerical algorithm are very similar to those in three dimensional ones. The test model with $a_0 = 3$ mm and $\lambda_0 = 60$ mm is calculated for a sequence of total grids 900×100, 1 800×200, 2 700×300 and 3 600×400. Fig. 3 shows the calculated amplitudes for different grid sizes. The largest relative error of amplitude is less than 0.8% at the late times. Therefore, the numerical solution is convergent for grids, and the computational domain is discretized with the grid refinement of 1 800×200, which corresponds to a grid size of 0.3 mm.

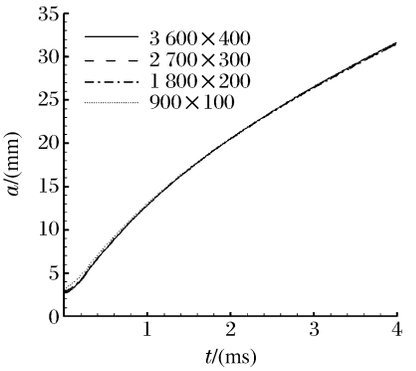


Fig. 3 Convergence test of two dimensional amplitude for grids

Table 2 Computational models

Wavelength/(mm)	Amplitude/(mm)	Wavelength/(mm)	Amplitude/(mm)	Wavelength/(mm)	Amplitude/(mm)
	1		6	30	
	2		8	40	
60	3	60	10	50	3
	4		12	70	
	5		14	80	

Fig. 4 and Fig. 5 show the comparisons of the amplitudes from numerical simulations with the predictions of impulsive model and nonlinear models of Zhang[5-7] and Sadot *et al*.[8] with fixed initial perturbation wavelength λ_0 and amplitude a_0. It can be seen that when the initial perturbation amplitude is relatively very small to the wavelength, the amplitude predicted by Zhang & Sohn nonlinear theory is the same as Sadot's prediction at the linear stage, and larger than it at the nonlinear stage (Fig. 4 (a)). When the initial amplitude increases gradually, the amplitude predicted by Zhang & Sohn nonlinear theory is smaller than the Sadot's prediction, and the difference also increases gradually. However, the predictions of the two nonlinear theories are always smaller than the results of the impulsive model. We define a parameter $P_S (= a_0/\lambda_0)$, which is the ratio of the initial amplitude to wavelength, to characterize the strength of initial perturbation. The Zhang & Sohn nonlinear theory is an asymptotic model and its predicted results have a constant asymptote, which is dependent on the strength of initial perturbation P_S. When the strength of initial perturbation P_S is small, the numerical calculated amplitude is consistent with the impulsive model at the linear stage and with the Zhang & Sohn model at both the linear and nonlinear stages (Fig. 4(a), Fig. 4(b) and Fig. 4(c), Fig. 5(d), Fig. 5(e) and Fig. 5(f)). While the initial perturbation strength P_S increases gradually, the impulsive model gives quantitatively incorrect prediction, the calculated results deflect from the Zhang & Sohn nonlinear theory at the beginning of nonlinear stage and gradually close up to the Sadot *et al*. nonlinear theory and intersect it, then deflect again. When the initial perturbation strength P_S is much larger, the nonlinear theory can not give the correct prediction of the RMI evolving.

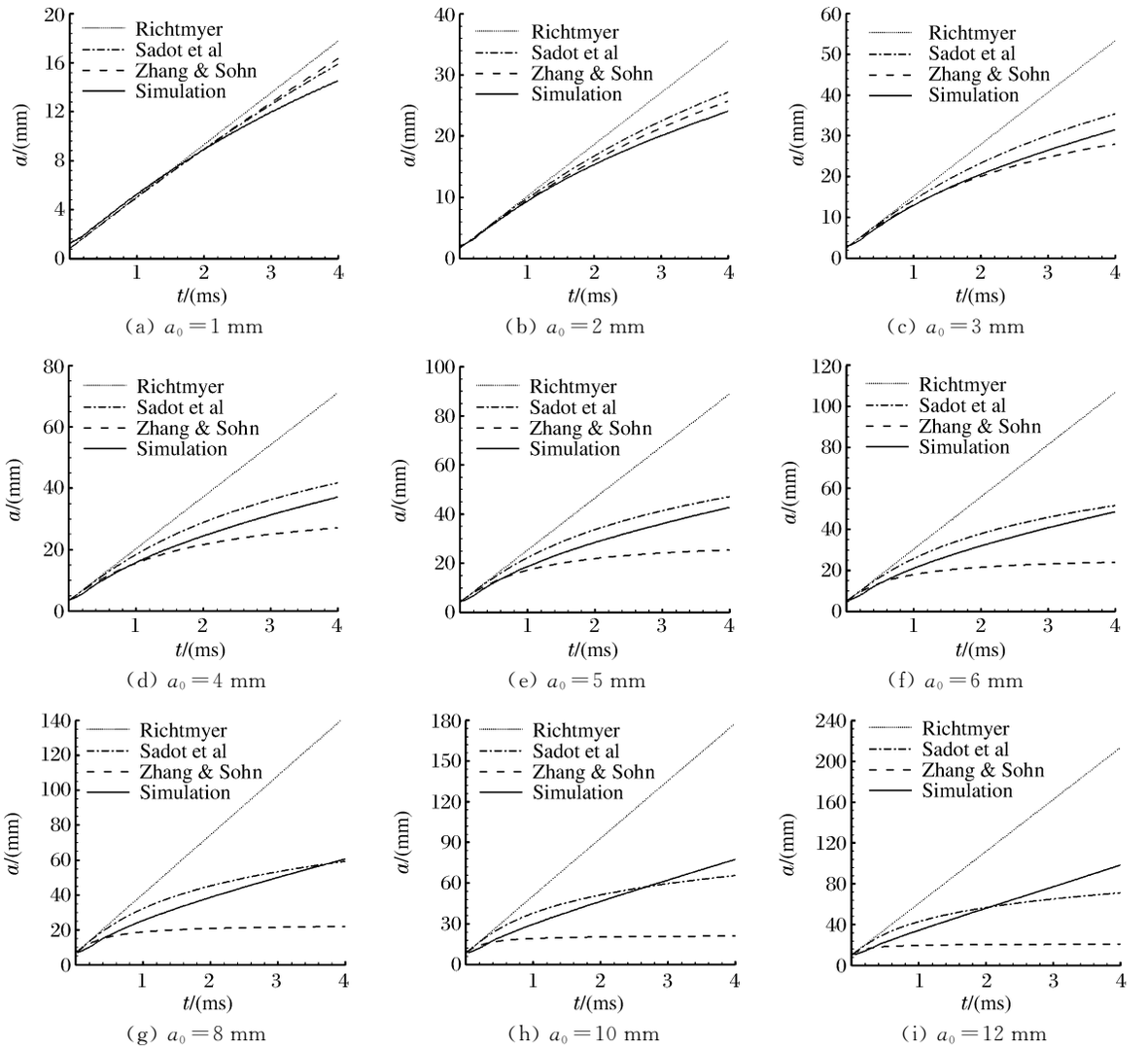
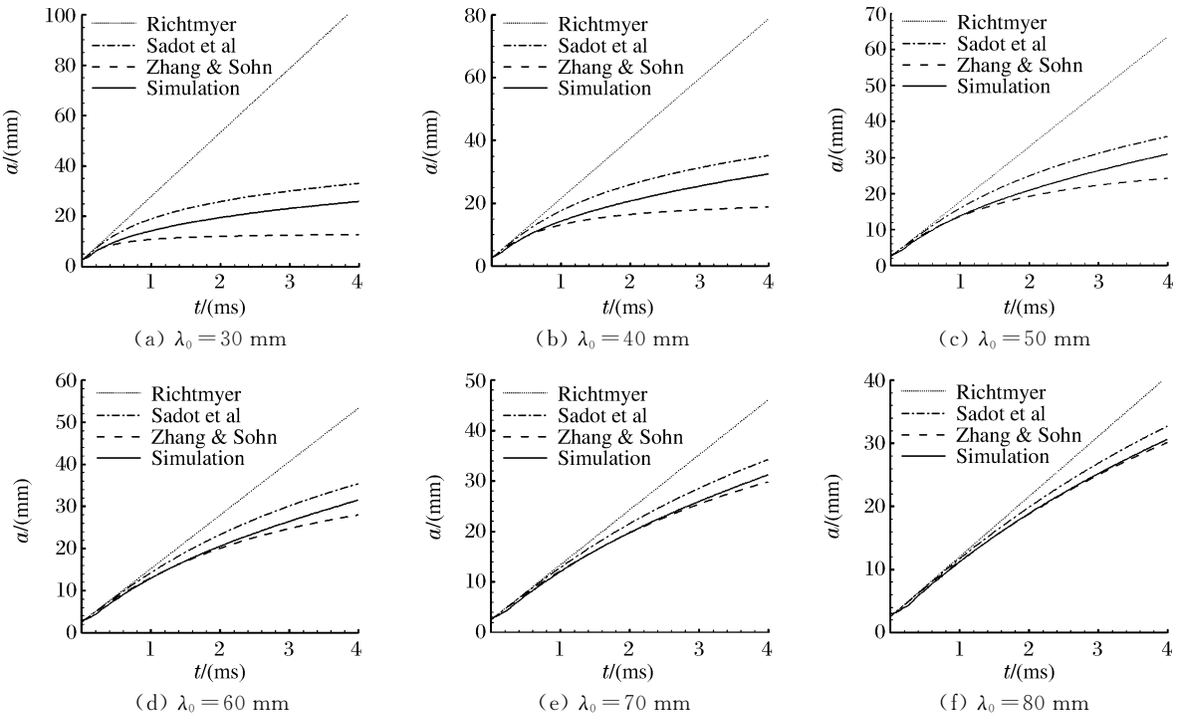


Fig. 4　Comparisons of the amplitudes from numerical simulations with the predictions of impulsive model, nonlinear theories of Sadot *et al*. and Zhang & Sohn, for the fixed initial perturbation wavelength λ_0=60 mm

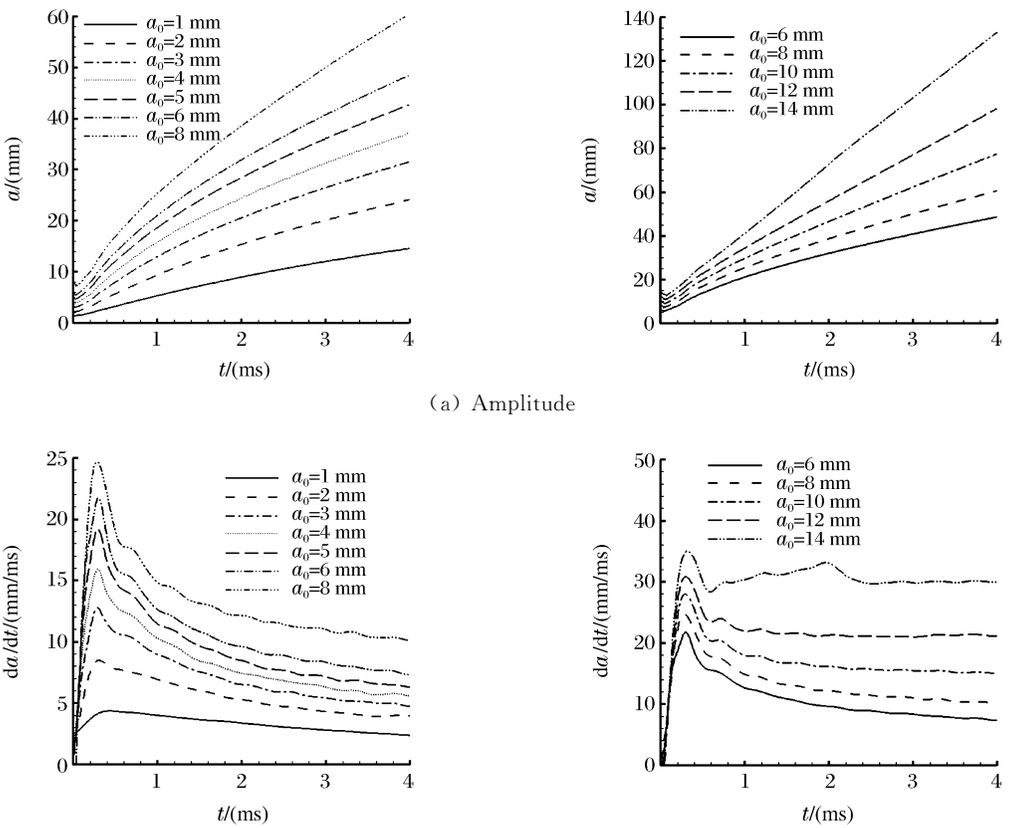
The comparisons of the numerically calculated amplitudes and growth rates for the fixed initial perturbation wavelength λ_0 = 60 mm and different initial amplitude are presented in Fig. 6(a) and Fig. 6(b), respectively. It can be concluded that the amplitude and growth rate increase gradually with the increasing of initial amplitude. When the initial amplitude is much larger, the calculated amplitude is increasing linearly at the late times, the growth rate remains a constant. The growth rate increases fast and reaches the highest peak at the early times. After the peak, the effect of compressibility is reduced and the nonlinearity starts to play a dominant role and causes the growth rate to decay with time. Fig. 6(b) demonstrates clearly that the system changes smoothly from a compressible and linear one to an incompressible and nonlinear one. Fig. 7(a) and Fig. 7(b) respectively present the comparisons of the numerically calculated amplitudes and growth rates for the fixed initial perturbation amplitude a_0=3 mm and different initial wavelength. We can see that the amplitude and growth rate reduce gradually at the early times and increase gradually at the late times with the increasing of initial wavelength. When the initial perturbation strength P_S is much smaller, the perturbation growth is mainly dependent on the initial perturbation amplitude and slightly dependent on the initial perturbation wavelength at the late times of RMI.



(a) $\lambda_0=30$ mm (b) $\lambda_0=40$ mm (c) $\lambda_0=50$ mm

(d) $\lambda_0=60$ mm (e) $\lambda_0=70$ mm (f) $\lambda_0=80$ mm

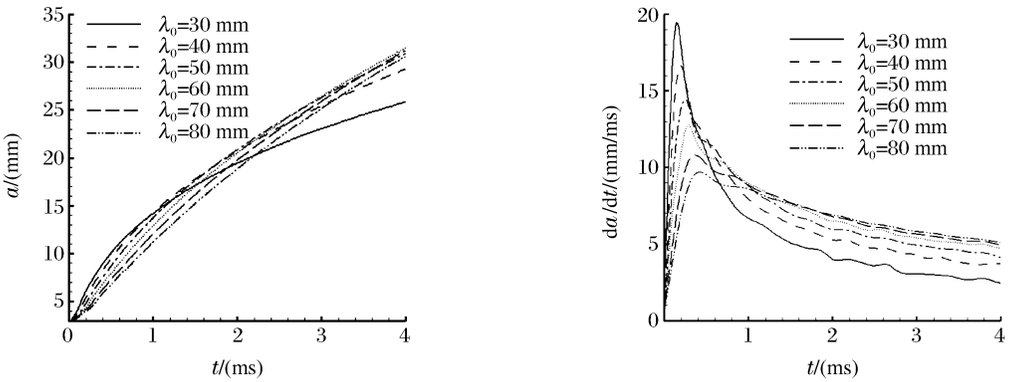
Fig. 5 Comparison of the amplitudes from numerical simulation with the predictions of impulsive model, Sadot *et al*. and Zhang & Sohn nonlinear theories for the fixed initial perturbation amplitude $a_0=3$ mm



(a) Amplitude

(b) Growth rate

Fig. 6 Comparison of the numerically calculated amplitudes and growth rates for the fixed initial perturbation wavelength $\lambda_0=60$ mm and different initial amplitude



(a) Amplitude　(b) Growth rate

Fig. 7　Comparison of the numerically calculated amplitudes and growth rates for the fixed initial perturbation amplitude $a_0 = 3$ mm and different initial wavelength

3.2　Three Dimensional Single-Mode RMI

In reality, the RMI often occurs in three dimensions (3D). Therefore, two calculations of three dimensional single-mode RMI are carried out. For the three dimensional single-mode RMI-1, the initial perturbed interface is in fact a two dimensional one which is stretched along the transverse (z) direction. And four models with the same initial perturbation wavelength $\lambda_0 = 60$ mm and different initial amplitudes $a_0 = 1, 2, 3, 4$ mm are calculated. The numerical results are almost same as the two dimensions. The three dimensional single-mode RMI-2 computational model and the initial perturbed interface are illustrated in Fig. 8, this is just the true three dimensional perturbation. The perturbed interface is given by

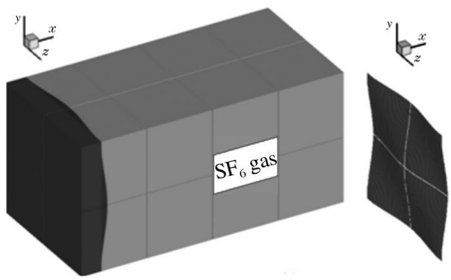


Fig. 8　3D-2 computational model and initial perturbed interface

$$x = x_0 + a_0 \sin(k_y y) \sin(k_z z) \tag{6}$$

where x_0 is the initial equilibrium position, a_0 is the initial amplitude, k_y and k_z are the transverse initial perturbation wavenumbers in y and z directions with $k_y = 2\pi/\lambda_{y,0}$ and $k_z = 2\pi/\lambda_{z,0}$ respectively, $\lambda_{y,0}$ and $\lambda_{z,0}$ are the transverse initial perturbation wavelengths. The efficient wavenumber in three dimensions is $k_{\text{eff}} = \sqrt{k_y^2 + k_z^2}$. In order to compare with the two dimensional results, the efficient wavenumber in three dimensions should be the same as the two dimensions.

In the 3D-2 simulations, the efficient initial perturbation wavelength is $\lambda_{\text{eff},0} = 60$ mm and the two transverse initial perturbation wavelengths $\lambda_{y,0}$ and $\lambda_{z,0}$ are the same, so $\lambda_{y,0} = \lambda_{z,0} = 85$ mm about. The size of computational domain is $[0, 680\text{ mm}] \times [0, 85\text{ mm}] \times [0, 85\text{ mm}]$ in (x, y, z) dimensions. The left and right boundaries in x direction are inflow/outflow boundaries, the upper and lower ones in y direction, the forward and backward ones in z direction are all periodic boundaries. The 3D-2 computational model is divided into 64 sub-zones (using $16 \times 2 \times 2$ CPUs) each with $100 \times 100 \times 100$ grids for parallel calculating. The conditions of incident shock and initial properties of materials are also the same as the two dimensions. Likewise, four models with different initial amplitude $a_0 = 1, 2, 3, 4$ mm are calculated.

Comparison of the amplitude from numerical simulation with the predictions of impulsive model, Sadot *et al*. and Zhang & Sohn nonlinear theories for the 3D-2 models is represented in Fig. 9. The same conclusion can be achieved. When the initial perturbation amplitude is relatively small to the wavelength, the numerical calculated amplitude agrees well with the impulsive model at the linear

stage and with the Zhang & Sohn nonlinear theory at both the linear and nonlinear stages. When the initial perturbation strength P_S increases gradually, the calculated amplitude gradually deflects from Zhang & Sohn nonlinear theory and consists with Sadot *et al*. nonlinear theory at the nonlinear stage. The predicted amplitude of three dimensional Zhang & Sohn nonlinear theory is larger than that of two dimensional one.

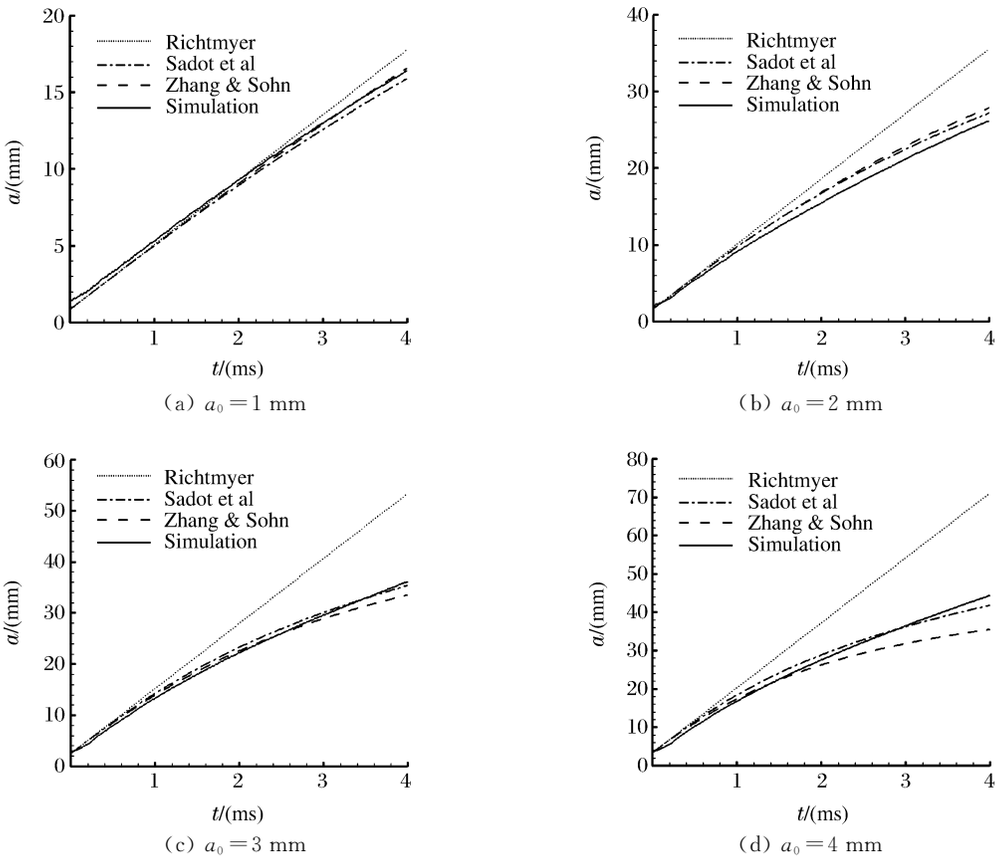


Fig. 9 Comparison of the amplitude from 3D-2 numerical simulation with the predictions of impulsive model, Sadot *et al*. and Zhang & Sohn nonlinear theories for the fixed efficient initial perturbation wavelength $\lambda_{eff,0}$ = 60 mm

3.3 Comparisons of 2D and 3D Results

Fig. 10 gives the comparisons of the 2 D , 3 D - 1 and 3 D - 2 numerically calculated amplitudes and growth

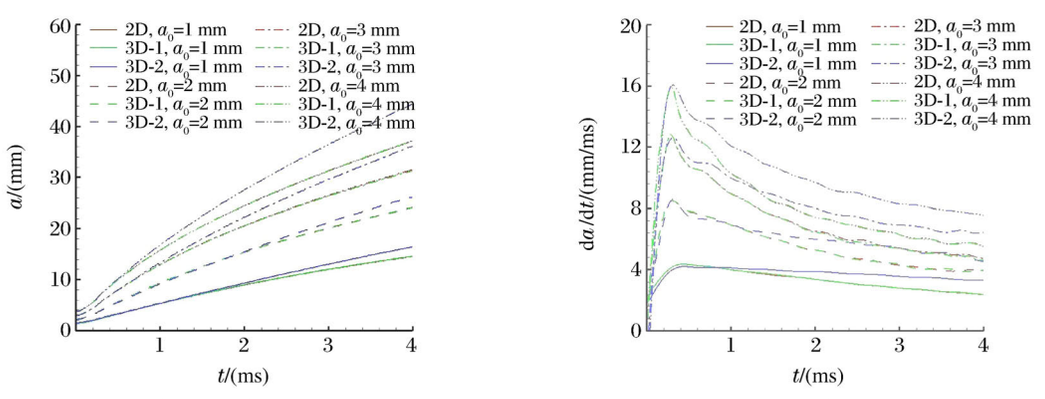


Fig. 10 Comparison of the 2D, 3D-1 and 3D-2 numerically calculated amplitudes and growth rates for the fixed initial perturbation wavelength λ_0 = 60 mm and different initial amplitude

rates for the fixed initial perturbation wavelength $\lambda_0 = 60$ mm and different initial amplitude $a_0 = 1, 2, 3, 4$ mm. It reveals that the 2D and 3D-1 calculated amplitudes have no difference from the linear to nonlinear stage, the 3D-2 calculated amplitudes are the same as 2D and 3D-1 ones at the linear stage and larger than those at the nonlinear stage, and the difference becomes greater with the increasing of initial perturbation strength. So do the growth rates. Therefore the effects of the nonlinearity and three dimensions play an important role in the development of RMI.

4 Conclusions

We carried out detailed simulations of the two and three dimensional single-mode RMI by using our high precision numerical algorithm MVPPM. Good agreements have achieved between the numerical simulations and the predictions of theory models for both two and three dimensions when the initial perturbation strength is small. The results also show that the evolving of perturbed interface is highly sensitive to the initial conditions of perturbation. The impulsive model can provide a quantitatively correct prediction of the RMI at the linear stage and the nonlinear theories can provide a quantitatively correct prediction of the RMI both at the linear stage and nonlinear stage. Our numerical algorithm can also realize correct numerical simulation of the RMI. The difference between two and three dimensional numerical results at the nonlinear stage shows that the effects of nonlinearity and three dimensions play an important role in the developing of RMI.

References:

[1] Richtmyer R D. Taylor instability in shock acceleration of compressible fluids [J]. Commun Pur Appl Math, 1960, 13(2): 297-319.

[2] Meshkov E E. Instability of the interface of two gases accelerated by a shock wave [J]. Sov Fluid Dyn, 1969, 4(5): 101-104.

[3] Zhang Q, Sohn S-Ik. Quantitative theory of Richtmyer-Meshkov instability in three dimensions [J]. Z angew Math Phys, 1999, 50(1): 1-46.

[4] Taylor G I. The instability of liquid surfaces when accelerated in a direction perpendicular to their planes [J]. Proc R Soc A, 1950, 201(1065): 192-196.

[5] Zhang Q, Sohn S-Ik. An analytical nonlinear theory of Richtmyer-Meshkov instability [J]. Phys Lett A, 1996, 212(3): 149-155.

[6] Zhang Q, Sohn S-Ik. Nonlinear theory of unstable fluid mixing driven by shock wave [J]. Phys Fluids, 1997, 9(4): 1106-1124.

[7] Li X L, Zhang Q. A comparative numerical study of the Richtmyer-Meshkov instability with nonlinear analysis in two and three dimensions [J]. Phys Fluids, 1997, 9(10): 3069-3077.

[8] Sadot O, Erez L, Alon U, et al. Study of nonlinear evolution of single-mode and two-bubble interaction under Richtmyer-Meshkov instability [J]. Phys Rev Lett, 1998, 80(8): 1654-1657.

[9] Meyer K A, Blewett P J. Numerical investigation of the stability of a shock-accelerated interface between two fluids [J]. Phys Fluids, 1972, 15(5): 753-759.

[10] Cloutman L D, Wehner M F. Numerical simulation of Richtmyer-Meshkov instabilities [J]. Phys Fluids A, 1992, 4(8): 1821-1830.

[11] Grove J W, Holmes R H, Sharp D H, et al. Quantitative theory of Richtmyer-Meshkov instability [J]. Phys Rev Lett, 1993, 71(21): 3473-3476.

[12] Holmes R H, Grove J W, Sharp D H. Numerical investigation of Richtmyer-Meshkov instability using front tracking [J]. J Fluid Mech, 1995, 301: 51-64.

[13] Zhang Z Z, Wang J H. Turbulent mixing model and numerical simulation of Richtmyer-Meshkov instability [J]. Explosion and Shock Waves, 1997, 17(3): 199-206. (in Chinese)
张忠珍, 王继海. k-D-a-B 模型和 Richtmyer-Meshkov 不稳定性的数值模拟 [J]. 爆炸与冲击, 1997, 17(3): 199-206.

[14] Srebro Y, Elbaz Y, Sadot O, et al. A general buoyancy-drag model for the evolution of the Rayleigh-Taylor and

Richtmyer-Meshkov instabilities [J]. Laser and Particle Beams, 2003, 21(3): 347-353.

[15] Yang M, Wang L L, Zhang S D, et al. The study of turbulent mixing induced by Richtmyer-Meshkov instability using turbulence model [J]. Acta Aerodynamica Sinica, 2010, 28(1): 119-123. (in Chinese)
杨 玟, 王丽丽, 张树道, 等. 用湍流模型研究 Richtmyer-Meshkov 不稳定性诱导的湍流混合 [J]. 空气动力学学报, 2010, 28(1): 119-123.

[16] Hill D J, Pantano C, Pullin D I. Large-eddy simulation and multiscale modeling of a Richtmyer-Meshkov instability with reshock [J]. J Fluid Mech, 2006, 557: 29-61.

[17] Thornber B, Drikakis D. Large-eddy simulation of shock-wave-induced turbulent mixing [J]. Journal of Fluid Engineering, 2007, 129(12): 1504-1513.

[18] Lombardini M, Deiterding R. Large-eddy simulation of Richtmyer-Meshkov instability in a converging geometry [J]. Phys Fluids, 2010, 22(9): 091112.

[19] Schilling O, Latini M, Don W S. Physics of reshock and mixing in single-mode Richtmyer-Meshkov instability [J]. Phys Rev E, 2007, 76(2): 026319(1)-026319(28).

[20] Latini M, Schilling O, Don W S. Effects of WENO flux reconstruction order and spatial resolution on reshocked two-dimensional Richtmyer-Meshkov instability [J]. J Comput Phys, 2007, 221: 805-836.

[21] Schilling O, Latini M. High-order WENO simulations of three-dimensional reshocked Richtmyer-Meshkov instability to late times: Dynamics, dependence on initial conditions, and comparisons to experimental data [J]. Acta Mathematica Scientia, 2010, 30B(2): 595-620.

[22] Zhang S. Adaptive mesh refinement and visiometrics in accelerated inhomogeneous flows [D]. New Jersey: The State University of New Jersey, 2004.

[23] Nourgaliev R R, Dinh T N, Theofanous T G. Adaptive characteristics-based matching for compressible multifluid dynamics [J]. J Comput Phys, 2006, 213(2): 500-529.

[24] Wang T, Bai J S, Li P, et al. The numerical study of shock-induced hydrodynamic instability and mixing [J]. Chin Phys B, 2009, 18(3): 1127-1135.

[25] Bai J S, Wang T, Zou L Y, et al. Numerical simulation for shock tube and jelly interface instability experiments [J]. Chinese Journal of Applied Mechanics, 2009, 26(3): 418-425. (in Chinese)
柏劲松, 王 涛, 邹立勇, 等. 激波管实验和果冻实验界面不稳定性数值计算 [J]. 应用力学学报, 2009, 26(3): 418-425.

单模态 RM 不稳定性的二维和三维数值计算研究

王 涛[1,2], 柏劲松[1], 李 平[1], 陶 钢[2], 姜 洋[1], 钟 敏[1]

(1. 中国工程物理研究院流体物理研究所, 四川绵阳 621900;
2. 南京理工大学能源与动力工程学院, 江苏南京 210094)

摘要: 发展了可用于可压缩多介质粘性流体动力学问题的数值模拟方法和代码 MVPPM (Multi-Viscous-Fluid Piecewise Parabolic Method)。利用 MVPPM 方法对多个具有不同初始扰动振幅和波长的二维和三维单模态 Richtmyer-Meshkov(RM)不稳定性模型进行了数值计算, 并和理论模型的计算结果进行了比较。结果显示, 扰动界面的发展与扰动的初始条件密切相关。无论二维还是三维情况, 当初始扰动强度较小的时候, 数值计算的扰动振幅及增长率和理论模型的计算结果一致。对于具有相同初始扰动的情况, 三维数值计算结果在线性段与二维计算结果相同, 但是在非线性段比二维结果大, 说明非线性和三维效应在 RM 不稳定性发展过程中起着重要作用。

关键词: MVPPM(Multi-Viscous-Fluid Piecewise Parabolic Method)方法; 单模态 Richtmyer-Meshkov 不稳定性; 非线性

中图分类号: O354; O357 **文献标识码:** A